DIII-D Research Advancing the Scientific Basis for Burning Plasmas and Fusion Energy

W.M. Solomon for the DIII-D team

General Atomics, San Diego, California 92121, USA

E-mail: solomon@fusion.gat.com

Abstract. The DIII-D tokamak has addressed key issues to advance the physics basis for ITER and future steady-state fusion devices. In work related to transient control, magnetic probing is used to identify a decrease in ideal stability, providing a basis for active instability sensing. Improved understanding of 3D interactions is emerging, with RMP-ELM suppression correlated with exciting an edge current driven mode. Should rapid plasma termination be necessary, shattered neon pellet injection has been shown to be tunable to adjust radiation and current quench rate. For predictive simulations, reduced transport models such as TGLF have reproduced changes in confinement associated with electron heating. A new wide-pedestal variant of QH-mode has been discovered where increased edge transport is found to allow higher pedestal pressure. New dimensionless scaling experiments suggest an intrinsic torque comparable to the beam-driven torque on ITER. In steady-state related research, complete ELM suppression has been achieved that is relatively insensitive to q_{95}, having a weak effect on the pedestal. Both high-$q_{\min}$ and hybrid steady-state plasmas have avoided fast ion instabilities and achieved increased performance by control of the fast ion pressure gradient and magnetic shear, and use of external control tools such as ECH. In the boundary, experiments have demonstrated the impact of $E \times B$ drifts on divertor detachment and divertor asymmetries. Measurements in helium plasmas have found that the radiation shortfall can be eliminated provided the density near the X-point is used as a constraint in the modeling. Experiments conducted with toroidal rings of tungsten in the divertor have indicated that control of the strike-point flux is important for limiting the core contamination. Future improvements are planned to the facility to advance physics issues related to the boundary, transients and high performance steady-state operation.

1. Introduction

Research on DIII-D [1] has made significant advances for fusion energy, with a focus on resolving issues critical to the success of ITER, while developing the operational knowledge and scientific basis relevant for next-step fusion devices. Progress has been made in the areas of transient control, transport physics, understanding of core-edge coupling and boundary processes, and integrated steady-state and inductive scenarios. Results described in this paper have been obtained by utilizing key developments in the facility (e.g. disruption mitigators, new diagnostics, very high harmonic fast wave ["helicon"] launch), as well as exploiting existing flexibility (e.g. shape control, independent variation of torque and power, decoupled ion and electron heating schemes, adjustable current drive deposition, variable applied 3D field spectra), and dedicated experimental campaigns with tungsten metal tile inserts and helium main ion and beam injection.

The paper is organized as follows. In Section 2, recent advances in the control of transient events, including both ELM control and mitigation of major disruptions is described, plus the first demonstration of runaway electron plateau dissipation using the shattered pellet technique. Section 3 describes research aimed at preparing for burning plasmas, including advances in the physics basis needed to achieve $Q = 10$ performance on ITER and improved understanding of the relevant transport processes. In Section 4, advances in the physics of detachment are presented, detailing the important role of drifts, together with new insights into the interplay between the divertor and upstream pedestal profiles. Finally, in Section 5, work focused on achieving steady-state performance for both ITER and future fusion reactors is discussed, with an emphasis on the integration of both the appropriate boundary solutions (ELM control and radiative divertor) and techniques for mitigating anomalous thermal and fast ion transport.

2. Control of Transient Events

2.1. Achieving high performance with robust ELM control

High confinement operation in H-mode is generally associated with strong gradients in the profiles near the edge, or so-called "pedestal" region. These strong gradients are observed to trigger edge localized modes (ELMs) [2], which result in repetitive bursts of energy and particles being expelled from the pedestal, and are a serious concern to the integrity of plasma facing components. While ELMs can be beneficial in present tokamaks by preventing impurity accumulation, in a burning plasma like ITER, the much larger energy content makes the periodic heat fluxes from ELMs a serious concern to the integrity of plasma facing components. DIII-D is pursuing several parallel lines of research to address this challenge, through the suppression of ELMs with resonant magnetic perturbations (RMP) [3], pellet pacing [4, 5], and naturally ELM-stable regimes such as Quiescent H-mode (QH-mode)[6].

New insights into the physics of RMP ELM suppression in ITER baseline conditions have been obtained providing more confidence in projecting to ITER. Measurements have revealed that ELM suppression is correlated with the magnitude of the plasma response driven on the high-field side (HFS) at low q_{95} on DIII-D, typical of ITER baseline conditions. The measured edge HFS response is found to be inversely proportional to the pedestal collisionality but with no dependence on β_N (Fig. 1), as would be expected for a current-driven kink mode. This is in contrast to the pressure-driven kink that depends on β_N and is observed on the low field side (LFS). Work remains to understand how to properly model the input equilibrium to predict experiments. Specifically, HFS modeling is revealed to be very sensitive to the details of the edge current profile and equilibrium truncation (which are not well measured) [7]. This issue is not unique to IPEC [8] modeling shown in Fig. 1. In contrast to issues identified with HFS modeling, all experimental LFS trends were well captured with both IPEC and MARS-F and reflects a more developed understanding of how to model LFS trends. Understanding mis-matches on the HFS is a frontier topic in plasma response and work is on-going to address this topic. The results demonstrated the importance of low collisionality for achieving ELM suppression [9] and supported the first achievement of ELM suppression at ASDEX Upgrade [10].

An emerging scientific picture to describe ELM suppression by RMP fields is that the expansion of the pedestal radially inward is halted by penetration of the field when the electron perpendicular drift velocity is low. This has been supported by measurements in L-mode plasmas showing island formation at the $q = 2$ surface from an applied field is easiest when the perpendicular electron velocity (as inferred using radial force balance, with ion measurements from charge exchange recombination spectroscopy and Thomson scattering measurements of the electrons) is near zero [11]. At the onset of ELM suppression, the plasma rotation and density fluctuation levels change rapidly, there is a transient increase in the divertor heat flux, and an additional striation is observed from visible emission on the inner wall. These changes are indicative of a bifurcation in the transport resulting from penetration of the fields. New experiments have found that ELM suppression can be achieved at low rotation and low β_N [12], but at higher β_N in ITER baseline conditions, ELM suppression is lost at reduced toroidal rotation. This is consistent with the need of low electron perpendicular drift velocity to allow field penetration, because co-current rotation is required to counteract the diamagnetic contribution to the flow. Hence, the achievement of ELM suppression in low rotation plasmas at low q_{95} likely requires the optimization of the edge intrinsic rotation drive, non-axisymmetric field-driven torques and the pedestal gradients, to ensure that the radial location of low perpendicular electron velocity is near the top of the pedestal as required [9].

As an alternative to actively suppressing ELMs, ITER will also be equipped to pace ELMs with D_2 pellets, aiming to increase the frequency of ELMs with a concomitant reduction in the peak heat flux. DIII-D has extended earlier studies of high frequency ELM pacing with D_2 pellets ($\approx$ 90 Hz or 8 times the natural ELM frequency) to

low rotation conditions anticipated for ITER. High frequency pacing has also been demonstrated with non-fuel Li pellets up to 200 Hz, resulting in a 10-fold increase in ELM frequency, at least transiently [13], as well as shown compatibility with core fueling. For Li pacing, most triggered ELM events show reductions in the heat flux, but a small fraction ($< 10\%$) show heat fluxes comparable to the natural un-paced ELMs.

Perhaps the most attractive solution to the ELM problem is to develop scenarios that are naturally ELM-stable with the required level of performance. QH-mode is one such candidate scenario, and has previously been reported at ITER levels of performance without ELMs [14, 15]. In QH-mode, the transport usually associated with ELMs is instead driven by an edge harmonic oscillation (EHO) that limits the pedestal to just below the peeling-ballooning stability limit. The EHO has previously been postulated to be a saturated kink-peeling mode destabilized by rotation shear. New modeling of a low-n EHO with the 3D resistive MHD code M3D-C1 finds a linear Eigenmode structure that shows good agreement with the experimental characteristics from magnetics and internal fluctuation diagnostics (Fig. 2), and confirms the importance of rotation shear in destabilizing the low-n EHO [16, 17]. Nonlinear simulations with JOREK [18] and NIMROD [19] produce a low-n saturated state with enhanced particle transport consistent with the experimental observations during QH-mode [20, 21].

Further advances have been made in the performance of low torque QH-mode at higher q_{95}. In particular, in a balanced double-null shape, the plasma is found to bifurcate to a new state at low torque, characterized by a significantly higher and wider pedestal (Fig. 3). The most recent experiments have demonstrated access to this state with essentially no early input torque. In these conditions, the wide pedestal QH-mode has achieved $\beta_N \approx 2.3$ and $H_{98(y,2)} \approx 1.6$. Measurements find that the $E \times B$ shear in the steep gradient region is reduced at low torque, which enables broadband turbulence to reduce the edge pressure gradients and, consequently, produce the wider pedestal [17, 22, 23]. Future work will investigate compatibility in single null ITER-like shapes and reduced q_{95}.

2.2. Disruption mitigation

If left unmitigated, full current disruptions would pose a serious threat to the integrity of the vessel components and first wall of ITER. A hierarchical approach is anticipated for preventing disruptions, by designing operating scenarios that minimize the risk of plasma termination, utilizing control schemes to avoid exceeding relevant stability limits, deploying techniques for safe ramp down such as locked mode spin up, and, where necessary, employing a disruption mitigation system (DMS) as a last line of defense. The DMS on ITER must simultaneously prevent damage from localized thermal losses during the thermal quench, excessive forces during the current quench, and effectively dissipate any runaway electron (RE) beams that may arise from the disruption.

DIII-D is uniquely equipped with the primary ITER DMS technology, shattered pellet injection (SPI), demonstrating thermal and current quench times that scale to

values required for ITER. Relative to massive gas injection (MGI), SPI has shown improved assimilation of the injected impurity species [24]. The first successful demonstration of RE plateau dissipation using SPI has been achieved [25], although changes in the composition of the pellet may be necessary to optimize dissipation properties. Separate experiments using a mixed species SPI technique show how the disruption properties can be tuned to optimize the trade-off in the radiation fraction and the current quench time (Fig. 4) [26].

Concerns have emerged regarding disruption mitigation in the presence of pre-existing MHD instabilities (e.g. rotating or locked magnetic islands), since the vast majority of experimental experience has been gained with disruptions triggered by the DMS in otherwise stable plasmas. New experiments on DIII-D show that both MGI and SPI techniques remain effective even in the presence of MHD instabilities, with no significant impact to mitigation of either the thermal or current quench loads [27]. In addition, particle assimilation is not degraded during the thermal quench, the radiation fraction is similar, and the injected impurities remain effective at accelerating the current decay.

DIII-D has deployed a new gamma ray imaging (GRI) diagnostic, a tangentially viewing pinhole camera, to make energy-resolved measurements of the incident gamma ray flux produced [28]. Inversion techniques are used to infer the RE distribution from the measured gamma ray flux. Energy-resolved measurements during controlled dissipation studies in quiescent runaway experiments show different growth and dissipation rates at different energies (Fig. 5), revealing that previously observed anomalous dissipation occurs at low energies [29]. However, higher energy runaway electrons transition to growth at approximately twice the critical electric field, more consistent with recent revisions to theory [30]. The cause for the anomalous loss at low energy is still under investigation, but one hypothesis is that it is due to magnetic fluctuation-driven radial transport.

3. Preparing for Burning Plasmas

3.1. Establishing the Basis for $Q = 10$ Performance in ITER Relevant Conditions

DIII-D is developing critical operational experience and scientific understanding to help ITER achieve its primary performance mission. To minimize the distance of extrapolation to ITER, DIII-D continues to extend scenarios toward more relevant conditions. In particular, recent work has focused on both increased heating through the electron transport channel and investigation of low torque stability and confinement.

A degradation in confinement is observed when ECH is added to ITER baseline (IBS) plasmas, associated with increases in both low and higher wavenumber density fluctuations as measured by the beam emission spectroscopy (BES) and Doppler back scattering (DBS) diagnostics. Power balance analysis shows a factor of two or greater increase in thermal ion and electron heat diffusivities (χ_i, χ_e) at radii outside the ECH deposition location (typically $\rho \approx 0.4$). New time-dependent transport simulations using

the trapped-gyro-Landau fluid (TGLF) [31] transport model successfully reproduce the observed changes in confinement resulting from an increase in intermediate- and high-k TEM- and ETG-scale turbulence, well-reproducing the electron density, electron temperature, and ion temperature profiles, and consistent with the fluctuation diagnostics [32, 33]. These predictions of significant electron transport driven by high-k fluctuations have been confirmed by direct nonlinear multi-scale gyrokinetic simulations [32]. When TGLF is used to predict particle transport for ITER, the balance of outward low-k and inward intermediate-k turbulent particle flux results in a peaked density profile, highlighting the need to also understand transport particle transport across spatial scales. Simulations with TGLF find the predicted fusion gain in ITER is below the $Q = 10$ target when assuming a flat density profile, but this can be recovered by including the predicted peaking of the density (although the impact on stability has not yet been investigated). The fusion gain can be increased further by exploiting higher pedestal density, which gives higher pedestal pressure and potentially even access to Super H-mode [34].

The ITER baseline scenario on DIII-D is typically challenged by low-n tearing modes, and at low torque there is a strong tendency for $m/n = 2/1$ tearing modes to slow and lock, often resulting in disruption. The differential rotation between the $q = 2$ and the $q = 3/2$ surface provides a partial separation of stable versus unstable time slices in a database of IBS discharges. In addition, at low torque and low rotation, the pedestal is typically found to be higher than in the standard co-NBI IBS, resulting in a modification to the bootstrap current and change in the overall current density profile shape at fixed total current. As a result, lower torque plasmas tend to be characterized by a current profile that is more "hollow" in the vicinity of the $q = 2$ surface. Unstable discharges tend to have a larger current gradient inside and outside of the $q = 2$ surface, while stable discharges tend to have a flatter current profile around $q = 2$ [33].

An extension of active MHD spectroscopy (AMS) to IBS conditions has revealed the approach toward an ideal stability limit at low rotation. The plasma magnetic response to a slowly rotating (≈ 20 Hz) $n = 1$ field increases a factor of two to three as the rotation is reduced, and the phase shows a sudden change at low rotation. Such a response is typical of AMS measurements when the plasma crosses an ideal MHD stability limit at high β. In these IBS plasmas, kinetic effects appear to be significant, with β_N only approximately half of the calculated no-wall limit. Modeling with the fully kinetic MARS-K model [35] with collisionality and resistivity, and the underlying equilibrium kept fixed, partially reproduces the amplitude response as the rotation is lowered, but do not yet capture the response at the lowest rotation levels (Fig. 6). Refinements to the collisionality model in the quasi-linear version MARS-Q [36] may improve the agreement at very low rotation [33]. In Fig. 7, one sees that the onset of a 2/1 instability is preceded by a significant increase in the plasma response as measured by real time sensors, illustrating the potential to use real-time measurements of the plasma response as part of a disruption warning and alarm system.

Adequate error field correction (EFC) is necessary to minimize unwanted field

penetration leading to rotating or locked tearing modes. While the critical amplitude for triggering 2/1 islands has been well documented for $n = 1$ fields [37, 38, 39], similar studies have not been reported for $n > 1$ fields. Recent measurements have indicated that locked mode thresholds for $n = 2$ are similar to $n = 1$ thresholds, with applied field amplitudes comparable to the intrinsic $n = 2$ error field on DIII-D able to trigger a locked $n = 2$ mode (Fig. 8). These $n = 2$ modes typically saturate within a few hundred milliseconds and are typically also accompanied by an $n = 1$ locked mode. The comparable sensitivity to $n = 2$ error fields and the multi-mode coupling between $n = 1$ and higher n's would imply a need for $n > 1$ error field correction using more than a single independently controlled toroidal array in ITER [40].

3.2. Improving transport understanding for projection to burning plasmas

Projecting the results from DIII-D to future burning plasma devices requires a solid physics basis. While there have been many important advances in the understanding of energy transport, it is now being realized that multi-scale turbulence must also be considered, and more attention is also being given to understanding momentum and particle transport.

A key uncertainty for projecting scenarios to future devices is the rotation, which can impact both confinement and stability. Because future large scale devices such as ITER are expected to rotate relatively more slowly from beam-injected torque than present day tokamaks, due to the rapid increase in moment of inertia with machine size, the intrinsic drive of rotation may play an important role. Dimensionless scaling experiments have suggested a more favorable ρ^* scaling of the intrinsic torque than expected from theoretical arguments (Fig. 9), and joint experiments with JET and ASDEX-Upgrade have confirmed this scaling [41, 42]. In addition, DIII-D experiments have shown a relatively weak scaling of intrinsic torque with ν^* [43]. These DIII-D results have been combined to yield a projection for the intrinsic torque in ITER that is comparable to the amount injected by neutral beams.

A flow reversal has been observed in the core of DIII-D L-mode plasmas when ECH is raised above a threshold power, which is correlated with the onset of ITG turbulence. New simulations with the Gyrokinetic Tokamak Simulation (GTS) code [44] accurately reproduce the observed toroidal rotation in the core resulting from a fluctuation-induced "residual stress" (Fig. 10) [42, 45]. Although these measurements and simulations are for L-mode, the gyro-Bohm normalized flux of residual stress in the core of an ITER H-mode may exceed that from the beam driven torque, and hence validation of the core residual stress is important for predicting the shear in the rotation profile, which, as noted earlier, can affect stability.

Experiments in hybrid plasmas have demonstrated that ECH power can help prevent the accumulation of argon injected by perturbative gas puff (i.e. impurity "flushing"), similar to previous observations on ASDEX-Upgrade [46]. Predictions of the argon profile evolution are made using STRAHL to calculate the Ar source, and

TGLF for the impurity transport coefficients. TGLF underpredicts the turbulent radial transport, resulting in higher argon accumulation and a more peaked argon density profile compared to the experiment [47]. In separate experiments where the temperature is held fixed while the torque is varied, the electron particle transport is affected by the $E \times B$ shearing rate when the shearing rate is below the linear growth rate [48]. The normalized density scale length $R\nabla n/n$ is well-correlated with the frequency of the dominant unstable mode, similar to previous observations on ASDEX-Upgrade [49], with the peaking maximized when the turbulence switches from ITG to TEM (Fig. 11). Nonetheless, core density peaking can be explained in some cases by increased core fueling from neutral beams, rather than specifically due to changes in collisionality [50]. Further study is needed to understand this observation in the context of multi-machine databases that show a strong increase in density peaking as the collisionality is reduced.

In general, an integrated approach to transport predictions is required, and theory-experiment validation efforts on DIII-D have increased the confidence in ITER achieving its $Q = 10$ mission. A self-consistent coupling of core and pedestal theoretical models has enabled global predictions of plasma performance to be made, without any free or fit parameters. An example of the agreement found in predicting the electron temperature profile is shown in Fig. 12 (a) [51, 52]. In this example, TGLF is used for the turbulent transport model in the core, NEO [53] is used for neoclassical transport, and with EPED [54, 55] providing the pedestal parameters that provide the "boundary conditions" to the TGLF model through a "transition region", and the solution is found using the transport solver TGYRO [56] within the "One modeling framework for integrated tasks" (OMFIT) framework [57]. Although not shown, excellent agreement is also achieved in the ion temperature and density. These simulations predict the global β_N, independent of the initial estimate, and does not take input from the experiment of the pressure at any radius in the plasma. Fig. 12 (b) also shows that regardless of the initial guess for β_N, the solution converges to a unique, self-consistent solution. In a large database of 200 discharges, this coupled modeling predicts the observed β_N to within 15%. Applied to ITER, paths to optimizing fusion gain up to $Q = 12$ have been found [52]. A new exciting frontier is now being explored with large multi-scale simulations that will lead to further improvements in the transport models and a better treatment of the balance of electron and ion transport [32, 58].

New studies on L-H transition physics finds that the L-H power threshold is minimized as a function of density for both hydrogen and deuterium plasmas when two counter-propagating broadband turbulence modes are present preceding the L-H transition [Fig. 13 (c)][59]. These modes are located just inside the separatrix, giving rise to an increase in poloidal flow shear that enhances turbulence suppression and facilitates the transition. In lower density L-mode plasmas (where the density is below the value corresponding to the minimum in the L-H power threshold), only the ion direction propagating mode is present [Fig. 13 (a)], while at higher densities, only the electron mode persists. In hydrogen plasmas, the appearance of the dual mode occurs at higher density than in deuterium plasmas, which would help explain the mass-dependence in

the power threshold. Across the L-H transition, the poloidal main ion flow acceleration is found to be quantitatively consistent with expectations from the turbulent Reynolds-stress across the entire edge shear layer [60]. Data from these studies are now being used to help constrain numerical models of the L-H transition.

4. Developing the Necessary Boundary Solutions for Fusion

4.1. Advances in physics of detachment

The Divertor Thomson Scattering (DTS) diagnostic has been used to show that drifts are responsible for in-out asymmetries and shifts in the radial profiles in the divertor leg, a result that is directly illustrated through the reversal of the toroidal field and associated $E \times B$ drifts. The measured temperature and density asymmetries have been reproduced with the UEDGE code [61] in H-mode discharges and point to the interplay between radial and poloidal $E \times B$ drifts, where poloidal drifts are responsible for the strong in-out asymmetries in H-mode (Fig. 14), while radial drifts shift the density profile [62].

Reversing the toroidal field is also found to lower the density for detachment in H-mode, illustrated by the plots of the peak temperature at the plate versus density in Fig. 15. Again, this can be understood due to the different role of $E \times B$ drifts, and indeed, modeling of these plasmas with UEDGE (not shown) is able to qualitatively reproduce this effect on the detachment threshold, provided full cross-field drifts are included. While other processes in the divertor such as electron heat conduction and recycling are critical for divertor modeling, it is becoming clear that complete quantitative predictions of partially detached divertor conditions and associated in-out asymmetries need to include drifts, and that future divertor designs might be better optimized by accounting for asymmetries due to drifts.

A persistent "radiation shortfall" has been found when performing divertor modeling, in both L- and H-mode deuterium plasmas. To investigate the role of atomic physics in the radiation shortfall, detachment experiments were performed in L-mode helium plasmas, which have reduced uncertainties compared to standard deuterium plasmas with carbon impurities because of the reduction of molecular deuterium and hydrocarbon reactions. Without direct measurement of the density in the divertor, the standard technique is to use the upstream density as a constraint to the divertor modeling. However, the DIII-D DTS diagnostic measures higher density throughout much of the divertor than indicated by SOLPS [63] modeling, as shown in Fig. 16. This under-prediction of the density contributes to an under-prediction of the radiations. Indeed, the radiation shortfall can be largely eliminated in helium plasma by taking a new approach to modeling the divertor, by matching the DTS-measured density near the X-point as a constraint. However, in order to produce a well-matched divertor, $\approx 50\%$ higher upstream density than is measured was needed in the modeling. This shows that parallel transport plays an important role in the radiation shortfall when upstream data are used to constrain the models, and suggests that the models may

be missing contributions to the total SOL pressure balance (e.g. underestimating ion contributions). Although the radiation shortfall can be eliminated in helium plasmas, the same is not true for deuterium plasmas, where increasing the upstream density only partially reduces the shortfall. This is consistent with previous results suggesting that inaccuracies in the models of molecular deuterium may contribute to the shortfall, and highlights the need to improve deuterium atomic and molecular physics in the modeling. Future experiments using the divertor SPRED spectrometer will further quantify these effects.

Measurements in unbalanced double-null plasmas biased toward the lower divertor ($dR_{sep} \approx 5$ mm) find that the peak heat flux at the outer divertor target of the primary divertor scales as $q_\perp \propto (P_{\rm SOL} I_p)^{0.92}$, where $P_{\rm SOL}$ is the power through the SOL, consistent with the ITPA scaling originating mostly from single null plasmas (Fig. 17). At very high power and $\beta_N > 3.7$, the addition of D_2 gas as part of a puff-and-pump radiative divertor is found to result in a more significant increase in density than typically observed, in part due to a reduction of the ELM frequency. This stronger effective core fueling sets an upper limit to the D_2 gas flow in DIII-D to maintain density control in a high β_N discharge with puff-and-pump radiative divertor, and may represent an additional challenge for the technique in very high performance plasmas. In these high β_N discharges, the energy confinement actually increases with D_2 gas flow, with β_N rising to nearly 4 at fixed power [64, 65].

The more advanced divertor geometry referred to as the X-divertor shows detachment at lower upstream density than standard divertor operation. At present, it is believed that the negative gradient in the poloidal field at the target (i.e. flaring) together with an increased connection length through the high neutral region at the target is responsible for facilitating this detachment at lower density.

A concern has emerged regarding the use of 3D fields (as might be envisioned for ELM control), because RMP fields had been observed to create lobes in the electron temperature that extend to the divertor plates (Fig. 18), as well as non-axisymmetric heat flux striations, which can lead to high levels of heat flux on less well-armored divertor regions. This has been a concern for ITER in using RMP fields for ELM suppression. However, new experiments on DIII-D have shown that these effects can be altered by typical dissipative processes at higher densities, where the electron temperature lobes move up, away from the targets. This occurs even before partial detachment begins. Therefore, partial detachment of the divertor may be sufficient to lower the temperature of particles striking the target plate in ITER, reducing sputtering, even when RMP fields are applied. The elimination of 3D effects occurs even though the effect on the particle confinement from the RMPs persists, as evidenced by the fact that higher fueling rates are required to maintain the same density, even above detachment. In EMC3-Eirene [66] simulations where only the density is varied, the observed reduction in non-axisymmetric divertor flux structures can be qualitatively reproduced. The reproduction of the observed trends demonstrate that EMC3-Eirene will be useful for understanding how current results are likely to scale to ITER operational scenarios with

RMPs, although it should be noted that changes in plasma response were not included in the simulations and remain an active area of research [67].

4.2. Interplay between divertor, SOL and pedestal

Comparison of the pedestal profile in the DIII-D closed upper divertor to the more open lower divertor shows that the more closed geometry exhibits an electron pedestal density profile with shallower gradient and lower height. This in turn results in a higher electron temperature pedestal (Fig. 19). Modeling shows that the more closed geometry results in a higher fraction of neutrals ionized in the divertor and a 30% reduction in the pedestal ionization source in otherwise similar divertor plasma conditions without auxiliary gas fueling. These differences remain even as the fueling is increased, such that the plasma detaches at pedestal densities 20% lower in the more closed divertor. While pedestal pressure and confinement tend to degrade under dissipative divertor operation, this appears to be a consequence of operating at higher collisionality, corresponding to a pedestal that is ballooning limited, and should be overcome in future devices operating at high density but low collisionality on the kink-peeling boundary [68].

4.3. Understanding material erosion and migration

Molybdenum and tungsten samples have been inserted into DIII-D using the Divertor Materials Evaluation System (DiMES) and have shown that the erosion rate is strongly influenced by carbon concentration in the plasma and the magnetic pre-sheath, and can be actively controlled with electrical biasing, as well as by local gas puffing. Modeling with the ERO code [69, 70], including a material mixing model, indicates that higher carbon concentration leads to more carbon deposition in the mixed material surface layer, which reduces the high-Z material erosion due to surface dilution [71]. $E \times B$ drifts directly impact the low-Z impurity transport and its deposition on high-Z material surfaces. The net erosion profiles on both Mo and W samples are well reproduced by ERO simulations assuming a carbon concentration of 1.8% (Fig. 20). New experiments show that Mo erosion can be reduced more than an order of magnitude when the biasing voltage is close to 40 V. The plasma density and temperature, controlled through localized gas puffing, can also modify the net erosion of high-Z material, as lower temperature and higher density result in a lower sputtering yield but higher carbon deposition in the surface [72].

New experiments have recently been performed using complete toroidal rings of W-coated metal inserts at two poloidal locations in the lower outer divertor [Fig. 21 (a)] to quantify high-Z divertor erosion and migration, together with the impact on core scenarios. The metal ring located on the shelf utilized an isotopically enriched ^{182}W to help distinguish the location for any observed metal influx. This was done using a new *ex-situ* analysis technique, inductively-coupled-plasma mass spectroscopy (ICP-MS), to quantify the deposition of the different W isotopes on an upstream midplane collector probe. In high power H-mode plasma, there is little evidence of any ^{182}W originating

from the shelf tile when measured at the collector probe, even with significant incident flux and source measured by direct filterscope view of the enriched tile, with nearly all the signal matching the natural W from the strike-point [Fig. 21 (b)]. This suggests that control of the strike-point flux is key to limiting the core contamination. In general, the W source was strongly impacted by the divertor characteristics, including ELM size, ELM frequency, flux expansion and location of the strike point. In high power, near-steady-state hybrid discharges, utilizing strong on-axis EC power for current drive, W accumulation was not observed, and the performance was essentially identical to cases without the metal rings [Fig. 22 (a)-(e)] . This is in contrast to other scenarios such as high-$q_{\min}$, which tends to use off- rather than on-axis EC power, resulting in significantly higher W concentrations [Fig. 22 (f)] as a consequence of losing the benefit from ECH "flushing" described in Sec. 3.2 that inhibits impurity accumulation [73]. More specifically, the ECH appears to lead to increased turbulent transport that flattens the density profile and reduces the inward neoclassical impurity pinch. The higher W concentration in the high-$q_{\min}$ plasmas often led to radiative collapse.

5. On the Path to Steady-State Operation

5.1. Development of High Performance Steady-State Scenarios

Significant advances have been made in developing an integrated core-edge solution for the steady-state hybrid regime. Previous work established it as a potentially attractive scenario, with simultaneous high $\beta_N \approx 3.7$ and high confinement $H_{98(y,2)} \approx 1.6$ achieved with zero loop voltage in a double null shape [74]. More recently, complete ELM suppression was achieved in plasmas using an ITER similar shape at $\beta_N \approx 3$ using odd parity $n = 3$ fields with only modest impact on performance ($\approx 5\%$ reduction in $H_{98(y,2)}$ and $\approx 10\%$ in pedestal pressure). Unlike at lower q_{95} for the IBS, ELM suppression is achieved over a wide range in q_{95} ($6 \lesssim q_{95} \lesssim 7.5$) in the steady-state hybrid (Fig. 23). Simulation suggests the scenario benefits from an increased plasma response due to the higher β_N, relative to the ITER baseline. New experiments have also demonstrated that high performance can be maintained with an argon puff-and-pump radiative divertor at $\beta_N \approx 3$, which enables radiated power above 50%, peak heat flux in the upper outer divertor reduced by a factor of two, and with less than a 10% increase in Z_{eff} and less than a 5% reduction in confinement [75].

Part of the attraction of the steady-state hybrid is that it can take advantage of on-axis current drive, with an anomalous process redistributing the current to give a broad q-profile associated with excellent confinement and stability. A new technique has been developed to quantify this process by comparing the poloidal flux driven by the coils and the poloidal flux converted to kinetic energy [76]. When there is no $m/n = 3/2$ tearing mode, the two measures of poloidal flux are in agreement and there is no anomaly in the current profile. However, in the presence of the mode, a difference emerges, sufficient to drive up to 10% of the current. Additional experiments and simulation utilizing applied 3D fields indicate this can arise due to a 3-wave interaction causing a helical distortion

of the plasma core [77].

Separately, a high bootstrap fraction, high β_P ($\lesssim 4$) scenario has been developed in collaboration with EAST [78], with a large radius internal transport barrier (ITB) operating fully non-inductively at $q_{95} \approx 12$ and maintaining good confinement and stability even at reduced torque [Fig. 24 (a)]. The scenario characteristics have also been maintained when the plasma current is increased inductively [Fig. 24 (b)], suggesting that a stable, fully non-inductive scenario at lower q_{95} should be feasible. New fluctuation measurements corroborate transport is predominantly neoclassical in this scenario, with no long wavelength turbulence detected. Turbulence is suppressed due to the large Shafranov shift (rather than $E \times B$ shear) in these high β_P plasmas. When β_P is ramped down by either reducing β_N or reducing q_{95}, the Shafranov shift stabilization is reduced, and the strong electron temperature ITB is eventually lost (Fig. 25) below a threshold. Both experiments and ideal stability calculations suggest that wall stabilization is important in this scenario, i.e. the ITB is observed to expand to larger radius at higher β_N, which in general improves the wall-stabilization and enables higher β_N. Projections to ITER suggest the high bootstrap fraction scenario will be fully non-inductive at lower $q_{95} \approx 6$, $\beta_P \approx 2.1$ and $\beta_N \approx 2.9$, and can potentially reach $Q = 5$ if confinement of $H_{98(y,2)} \approx 1.6$ is achieved. Analysis suggests this might be feasible, by maintaining the Shafranov shift with a stronger reverse shear current profile to compensate the lower β_P [79].

In separate high-$q_{\min}$ experiments at lower q_{95}, high confinement ($H_{98(y,2)} \approx 1.5$) and improved stability up to $\beta_N \approx 4$ is achieved when $q_{\min} > 2$ and with negative central shear (NCS). These are limited in β by the ideal wall stability limit as predicted by MHD theory, provided other instabilities including resistive wall modes and tearing modes are avoided. Stability analysis indicates higher limits are possible at lower ℓ_i [80], validating the planned path for further improvement through off-axis current drive. To further this goal in a reactor, DIII-D is also exploring very high harmonic fast waves ("helicon") at 476 MHz in plasmas with high electron β [81]. An initial low power test of a comb-line type antenna with 12 modules revealed good coupling, and research is ready to proceed to a 1 MW system to test non-linear dynamics [82].

5.2. Control of thermal and fast ion transport

New experiments demonstrate that a broad current profile incorporating NCS is effective in mitigating confinement degradation associated with increasing the electron to ion temperature ratio T_e/T_i, with the T_i profile maintained as ECH is added, unlike observations in standard positive shear plasmas. The difference can be explained in terms of the turbulence, with both simulations and measurements showing that increases in T_e/T_i have less impact on the fluctuation levels in NCS plasmas (Fig. 26) [83].

In high $q_{\min}$ plasmas, increased fast ion transport has been observed, which is now understood to be the result of multiple unstable Alfvén Eigenmodes that can lead to "stiff" fast ion transport above a critical gradient. The rapid increase in

fast ion transport observed with increasing power is well correlated with the degree of stochasticity of the fast ion orbits resulting from the overlapping modes, as calculated with the ORBIT [84] code, as shown in Fig. 27 (a). In addition, intermittent losses are observed to increase with beam power above the threshold [Fig. 27 (b)], and the fast ion density profile remains relatively unchanged even as the source power is increased [85, 86]. In such cases, the neutron rate is over-predicted by TRANSP [87] using classical slowing down and pitch angle scattering. A new phase-space resolved "kick-model" [88] has been developed and implemented in TRANSP to take into account the resonant effects of multiple modes and the fast ions. With this improved model, the neutron rate is accurately reproduced (Fig. 28) [89]. The poor fast ion confinement is calculated to be a consequence of an undesirable alignment between the fast ion pressure gradient and $q_{\min}$, and both simulations and experiments show that moving $q_{\min}$ to larger radius, where the fast ion pressure gradient is less steep, can effectively mitigate the anomalous fast ion transport, an effect that appears to be in play in the high β_P scenario. This further validates the path for broadening the current to develop high performance scenarios.

In the steady-state hybrid scenario, the addition of central ECCD suppresses fast ion instabilities, somewhat similar to previous work that found a dramatic impact on Alfvén Eigenmode activity when EC power is deposited in the vicinity of the location of $q_{\min}$. In cases with reverse magnetic shear, careful studies have revealed that finite temperature effects can explain the impact of EC power on Alfvén Eigenmode stability. A model was developed constraining the Reverse Shear Alfvén Eigenmode (RSAE) frequency sweep between a minimum frequency for the RSAE $f_{\mathrm{RSAE,min}}$ [related to the geodesic acoustic mode (GAM) frequency with a correction associated with the temperature gradient] and the Toroidal Alfvén Eigenmode (TAE) frequency f_{TAE}, implying RSAEs are not observed when the $f_{\mathrm{RSAE,min}} \geq f_{\mathrm{TAE}}$. This model successfully distinguishes between plasmas with strong TAE+RSAE activity versus those with a spectrum of TAE fluctuations, across a wide database of DIII-D discharges [90, 91]. A specific example shown for two discharges with and without ECH deposited near $q_{\min}$ is shown in Fig. 29. In the case with ECH, $f_{\mathrm{RSAE,min}} > f_{\mathrm{TAE}}$ and there are no frequency-sweeping RSAEs observed, as expected from this model (although strong TAE activity is still permitted and indeed observed). Due to the fact that the number of modes, their frequency, spatial extent and amplitude can impact AE-induced energetic particle (EP) transport, modifying the AE activity from combined RSAE and TAEs to purely TAEs does not necessarily cause an improvement in fast ion confinement. TAEs are often more effective than RSAEs at causing EP transport due to their higher poloidal harmonic content and potentially larger radial extent, often extending to the plasma edge in DIII-D plasmas [92]. Consistent with this picture, previous experiments with ECH "stabilized" RSAEs, but a remaining spectrum of TAEs, showed modest improvements in EP confinement yet still had significant neutron deficits [93].

6. Summary and Future Plans

This paper has described key advances in understanding, and demonstration of important principles necessary for the path to realizing fusion energy. RMP-ELM suppression is found to be correlated with exciting an edge current driven mode, while core tearing mode drives are mediated through a global kink response. A more complete understanding of QH-mode has been developed, with modeling confirming the EHO as a saturated kink-peeling instability destabilized by $E \times B$ shear. Shattered pellet injection, the technique selected for disruption mitigation on ITER, has demonstrated runaway electron dissipation for the first time and shown improved impurity assimilation compared with massive gas injection.

Stability remains a challenge for the IBS on DIII-D at low torque, where $m/n = 2/1$ tearing modes are generally observed to be triggered. Active MHD spectroscopy has been successful in detecting the approach to ideal instability in the low torque IBS, which appears to be a precursor to the 2/1 instability. New studies show a more favorable ρ^* scaling for the intrinsic rotation drive than might be expected from theory, giving rise to a torque that may be comparable to that from neutral beams on ITER. ECH power is found useful for preventing accumulation of both moderate- and high-Z impurities.

New diagnostic capability has shown the critical role of drifts in driving in-out asymmetries in the divertor legs. The previously observed "radiation shortfall" is largely eliminated in helium plasmas, provided that the divertor density is reproduced. Therefore, improvements in the parallel transport and atomic/molecular physics are needed to resolve the radiation shortfall in the modeling. 3D striations observed in the divertor with applied RMPs are eliminated at higher density approaching detachment.

ELM-suppression has been achieved in fully non-inductive steady-state hybrid plasmas, with relative insensitivity to q_{95}, and only small impact on confinement and performance. The high β_P scenario maintains high confinement levels even at low levels of torque, understood by the fact that the turbulence is suppressed by high β Shafranov stabilization. Anomalous fast ion transport is understood to result from stiff transport above a critical gradient, which can be overcome by moving the location of $q_{\min}$ to larger radius.

Future plans include a modification to the upper divertor on DIII-D for testing several principles of closure, as well as exploiting a new optimized geometry dubbed "small angle slot" (SAS) that aims to achieve detachment at reduced upstream density and lower temperatures across the entire target, important for an advanced divertor solution. A second SPI system using a three-barrel ITER prototype design [94] is currently being installed on DIII-D, which will allow investigation of pellet synchronization and multiple pellet injections from toroidally distinct locations to provide valuable information in preparation for operation on ITER. New power supplies have been provided through a collaboration with ASIPP that will enable increased flexibility of 3D coils for improved transient control. During a planned long torus opening beginning in the latter half of 2017, a second neutral beam line will be modified

to deliver additional off-axis current drive, which together with increased ECCD power will be exploited to push toward a fully non-inductive high $q_{\min} \approx 2$ scenario with $\beta_N \gtrsim 4.5$ to help resolve the path to steady-state. There is also a plan to further validate the helicon approach for driving off-axis current with a high power antenna installation.

This work was supported by the US Department of Energy under DE-FC02-04ER54698. DIII-D data shown in this paper can be obtained in digital format by following the links at `https://fusion.gat.com/global/D3D_DMP`.

[1] BUTTERY, R., Nucl. Fusion **55** (2015) 104017.
[2] ZOHM, H., Plasma Phys. Control. Fusion **38** (1996) 105.
[3] EVANS, T. E., MOYER, R. A., THOMAS, P. R., et al., Phys. Rev. Lett. **92** (2004) 235003.
[4] LANG, P. T., NEUHAUSER, J., HORTON, L. D., et al., Nucl. Fusion **43** (2003) 1110.
[5] BAYLOR, L., COMBS, S., FOUST, C., et al., Nucl. Fusion **49** (2009) 085013.
[6] BURRELL, K. H., AUSTIN, M. E., BRENNAN, D. P., et al., Phys. Plasmas **8** (2001) 2153.
[7] PAZ-SOLDAN, C., LOGAN, N., HASKEY, S., et al., Nucl. Fusion **56** (2016) 056001.
[8] PARK, J.-K., BOOZER, A. H., and GLASSER, A. H., Phys. Plasmas **14** (2007) 052110.
[9] PAZ-SOLDAN, C., NAZIKIAN, R., MOYER, R., and CALLEN, J., "Optimization of the Plasma Response for the Control of Edge-Localized Modes with 3D Fields", Preprint: 2016 IAEA Fusion Energy Conference, Kyoto, paper EX/1-2 .
[10] NAZIKIAN, R. M., PAZ-SOLDAN, C., SUTTROP, W., and KIRK, A., "First observation of ELM suppression by magnetic perturbations in ASDEX Upgrade in a shape-matching identity experiment with DIII-D", Preprint: 2016 IAEA Fusion Energy Conference, Kyoto, paper EX/PD-1 .
[11] SHAFER, M. W., CANIK, J. M., EVANS, T. E., and FERRARO, N. M., "Validating Extended MHD Models of Plasma Response Against Measurements of Islands in DIII-D", submitted to Nuclear Fusion .
[12] EVANS, T. E., LOARTE, A., ORLOV, D. M., et al., "ELM suppression in helium plasmas with 3D magnetic fields" submitted to Nuclear Fusion .
[13] BORTOLON, A., BAYLOR, L. R., MAINGI, R., and MANSFIELD, D. K., "Effectiveness of high-frequency ELM pacing with deuterium and non-fuel pellets in DIII-D", Preprint: 2016 IAEA Fusion Energy Conference, Kyoto, paper EX/10-1 .
[14] GAROFALO, A. M., BURRELL, K. H., ELDON, D., et al., Phys. Plasmas **22** (2015) 056116.
[15] SOLOMON, W. M., BURRELL, K. H., FENSTERMACHER, M. E., et al., Nucl. Fusion **55** (2015) 073031.
[16] CHEN, X., BURRELL, K., FERRARO, N., et al., Nucl. Fusion **56** (2016) 076011.
[17] CHEN, X., BURRELL, K. H., OSBORNE, T. H., and BARADA, K., "Bifurcation of Quiescent H-mode to a Wide Pedestal Regime in DIII-D and Advances in the Understanding of Edge Harmonic Oscillations", submitted to Nuclear Fusion .
[18] HUYSMANS, G. and CZARNY, O., Nucl. Fusion **47** (2007) 659.
[19] SOVINEC, C. R., GLASSER, A. H., GIANAKON, T. A., et al., J. Comput. Phys. **195** (2004) 355.
[20] LIU, F., HUIJSMANS, G. T. A., LOARTE, A., et al., "Nonlinear MHD simulations of Quiescent H-mode pedestal in DIII-D", Preprint: 2016 IAEA Fusion Energy Conference, Kyoto, paper TH/P1-9 .
[21] KING, J., "Nonlinear extended-MHD modeling by the NIMROD code of broadband-MHD turbulence during DIII-D QH-mode discharges", Preprint: 2016 IAEA Fusion Energy Conference, Kyoto, paper TH/P1-8 .
[22] BURRELL, K. H., BARADA, K., CHEN, X., et al., Phys. Plasmas **23** (2016) 056103.
[23] CHEN, X., BURRELL, K., OSBORNE, T., et al., Nucl. Fusion **57** (2017) 022007.
[24] COMMAUX, N., SHIRAKI, D., BAYLOR, L., et al., Nucl. Fusion **56** (2016) 046007.
[25] COMMAUX, N., SHIRAKI, D., BAYLOR, L. R., and EIDIETIS, N. W., "Shattered Pellet Injection as the Primary Disruption Mitigation Technique for ITER", Preprint: 2016 IAEA Fusion Energy Conference, Kyoto, paper EX/9-2 .
[26] SHIRAKI, D., COMMAUX, N., BAYLOR, L. R., et al., Phys. Plasmas **23** (2016) 062516.
[27] SHIRAKI, D., GRANETZ, R. S., COMMAUX, N., and BAYLOR, L. R., "Disruption Mitigation in the Presence of Pre-existing MHD Instabilities", Preprint: 2016 IAEA Fusion Energy Conference, Kyoto, paper EX/P3-20 .
[28] PACE, D. C., COOPER, C. M., TAUSSIG, D., et al., Rev. Sci. Instrum. **87** (2016) 043507.
[29] PAZ-SOLDAN, C., EIDIETIS, N. W., GRANETZ, R., et al., Phys. Plasmas **21** (2014) 022514.

[30] ALEYNIKOV, P. and BREIZMAN, B. N., Phys. Rev. Lett. **114** (2015) 155001.
[31] STAEBLER, G. M., KINSEY, J. E., and WALTZ, R. E., Phys. Plasmas **12** (2005) 102508.
[32] HOLLAND, C., HOWARD, N. T., and GRIERSON, B. A., "Demonstrating the Multi-scale Nature of Electron Transport Through Experimentally Validated Simulations", submitted to Nuclear Fusion .
[33] TURCO, F., LUCE, T. C., HANSON, J. M., and GRIERSON, B. A., "Current density and rotation profiles govern the stability of the ITER Baseline Scenario in DIII-D; predictive transport simulations capture the confinement degradation due to direct electron heating", Preprint: 2016 IAEA Fusion Energy Conference, Kyot .
[34] SOLOMON, W. M., SNYDER, P. B., BORTOLON, A., et al., Phys. Plasmas **23** (2016) 056105.
[35] LIU, Y., CHU, M. S., GIMBLETT, C. G., and HASTIE, R. J., Phys. Plasmas **15** (2008) 092505.
[36] LIU, Y., KIRK, A., and SUN, Y., Phys. Plasmas **20** (2013) 042503.
[37] LA HAYE, R. J., FITZPATRICK, R., HENDER, T. C., et al., Phys. Fluids B **4** (1992) 2098.
[38] BUTTERY, R., BENEDETTI, M. D., GATES, D., et al., Nucl. Fusion **39** (1999) 1827.
[39] WOLFE, S. M., HUTCHINSON, I. H., GRANETZ, R. S., et al., Phys. Plasmas **12** (2005) 056110.
[40] LANCTOT, M., PARK, J.-K., PIOVESAN, P., et al., to be submitted to Phys. Plasmas (2016) .
[41] TALA, T., CHRYSTAL, C., MCDERMOTT, R., PEHKONEN, S.-P., and SALMI, A., 43rd European Physical Society Conference on Plasma Physics (2016) .
[42] GRIERSON, B. A., WANG, W. X., CHRYSTAL, C., and DEGRASSIE, J. S., "Validation of Theoretical Models of Intrinsic Torque in DIII-D and Projection to ITER by Dimensionless Scaling", Preprint: 2016 IAEA Fusion Energy Conference, Kyoto, paper EX/11-1 .
[43] CHRYSTAL, C., GRIERSON, B., SOLOMON, W., and TALA, T., submitted to Phys. Plasmas (2016) .
[44] WANG, S., Phys. Rev. Lett. **97** (2006) 085002.
[45] GRIERSON, B. A., WANG, W., ETHIER, S., et al., Phys. Rev. Lett. **118** (2017) 015002.
[46] DUX, R., NEU, R., PEETERS, A. G., et al., Plasma Phys. Control. Fusion **45** (2003) 1815.
[47] GRIERSON, B. A., BURRELL, K. H., NAZIKIAN, R. M., et al., Phys. Plasmas **22** (2015) 055901.
[48] WANG, X., MORDIJCK, S., ZENG, L., et al., Plasma Phys. Control. Fusion **58** (2016) 045026.
[49] ANGIONI, C., CAMENEN, Y., CASSON, F. J., et al., Nucl. Fusion **52** (2012) 114003.
[50] MORDIJCK, S., WANG, X., ZENG, L., and RHODES, T. L., "Dominant role of turbulence in determining particle transport and confinement", Preprint: 2016 IAEA Fusion Energy Conference, Kyoto, paper EX/P3-9 .
[51] MENEGHINI, O., SNYDER, P. B., SMITH, S. P., et al., Phys. Plasmas **23** (2016) 042507.
[52] MENEGHINI, O., SNYDER, P. B., CANDY, J., and STAEBLER, G. M., "Development of a First-Principles Self-Consistent Core-Pedestal Model and its Application to ITER", submitted to Nuclear Fusion (2016).
[53] BELLI, E. A. and CANDY, J., Plasma Phys. Control. Fusion **50** (2008) 095010.
[54] SNYDER, P. B., GROEBNER, R. J., LEONARD, A. W., OSBORNE, T. H., and WILSON, H. R., Phys. Plasmas **16** (2009) 056118.
[55] SNYDER, P., GROEBNER, R., HUGHES, J., et al., Nucl. Fusion **51** (2011) 103016.
[56] CANDY, J., HOLLAND, C., WALTZ, R. E., FAHEY, M. R., and BELLI, E., Phys. Plasmas **16** (2009) 060704.
[57] MENEGHINI, O., SMITH, S. P., LAO, L. L., et al., Nucl. Fusion **55** (2015) 083008.
[58] STAEBLER, G. M., SNYDER, P. B., CANDY, J., and WALTZ, R. E., "A Model of The Saturation of Electron and Ion Scale Gyrokinetic Turbulence ", submitted to Nuclear Fusion (2016).
[59] YAN, Z., GOHIL, P., MCKEE, G. R., and ELDON, D., "Turbulence and Sheared Flow Structures Behind the Isotopic Dependence of the L-H Power Threshold and H-L Back Transition on DIII-D", Preprint: 2016 IAEA Fusion Energy Conference, Kyoto, paper EX/5-1 .
[60] SCHMITZ, L., GRIERSON, B. A., RHODES, T. L., and YAN, Z., "Turbulence-Flow Coupling and Poloidal Main-Ion Flow Acceleration Preceding the L-H Transition", Preprint: 2016 IAEA

Fusion Energy Conference, Kyoto, paper EX/P3-11 .

[61] ROGNLIEN, T. D., RYUTOV, D. D., MATTOR, N., and PORTER, G. D., Phys. Plasmas **6** (1999) 1851.

[62] MCLEAN, A. G., ROGNLIEN, T. D., CANIK, J. M., and ALLEN, S. L., "The Role of Drifts and Radiating Species in Detached Divertor Operation at DIII-D", submitted to Nuclear Fusion .

[63] SCHNEIDER, R., BONNIN, X., BORRASS, K., et al., Contributions to Plasma Physics **46** (2006) 3.

[64] PETRIE, T. W., ALLEN, S. L., FENSTERMACHER, M. E., and GUO, H. Y., "Edge- and Divertor Plasma Behavior in High Power High Performance Double-null Plasmas", submitted to Nuclear Fusion .

[65] PETRIE, T., FENSTERMACHER, M., HOLCOMB, C., et al., Nuclear Materials and Energy **0** (2016) 1.

[66] FENG, Y., SARDEI, F., KISSLINGER, J., and GRIGULL, P., J. Nucl. Mater. **241-243** (1997) 930.

[67] BRIESEMEISTER, A. R., AHN, J.-W., CANIK, J. M., and FENSTERMACHER, M. E., "Elimination of the Non-Axisymmetric inter-ELM Heat Flux Generated by Resonant Magnetic Perturbations in Detached Divertor Conditions", submitted to Nuclear Fusion .

[68] LEONARD, A. W., GROEBNER, R. J., MAKOWSKI, M. A., and MCLEAN, A. G., "Robust H-mode Pedestal Compatibility with SOL and Divertor Plasma Constraints", submitted to Nuclear Fusion .

[69] NAUJOKS, D., BEHRISCH, R., COAD, J., and KOCK, L. D., Nucl. Fusion **33** (1993) 581.

[70] KIRSCHNER, A., PHILIPPS, V., WINTER, J., and KÖGLER, U., Nucl. Fusion **40** (2000) 989.

[71] DING, R., STANGEBY, P., RUDAKOV, D., et al., Nucl. Fusion **56** (2016) 016021.

[72] DING, R., RUDAKOV, D. L., STANGEBY, P. G., and WAMPLER, W., "Advances in Understanding of High-Z Material Erosion and Re-deposition in Low-Z Wall Environment in DIII-D", Preprint: 2016 IAEA Fusion Energy Conference, Kyoto, paper MPT/1-2Rb .

[73] UNTERBERG, E. A., ABRAMS, T., ALLEN, S. L., and BAYLOR, L. R., "Characterization of Divertor Tungsten Sourcing and Transport into the SOL and Core for DIII-D ELM-y H-mode Conditions", submitted to Nuclear Fusion .

[74] TURCO, F., PETTY, C. C., LUCE, T. C., et al., Phys. Plasmas **22** (2015) 056113.

[75] PETTY, C. C., NAZIKIAN, R. M., TURCO, F., and CHEN, X., "Advances in the Steady-State Hybrid Regime in DIII-D - a Fully-Noninductive, ELM-Suppressed Scenario for ITER", submitted to Nuclear Fusion .

[76] LUCE, T. C., HUMPHREYS, D. A., JACKSON, G. L., and SOLOMON, W. M., Nucl. Fusion **54** (2014) 093005.

[77] PIOVESAN, P., TURCO, F., LIU, Y. Q., and WILCOX, R. S., "Role of MHD dynamo in the formation of 3D equilibria in fusion plasmas", Preprint: 2016 IAEA Fusion Energy Conference, Kyoto, paper EX/1-1 .

[78] GAROFALO, A. M., GONG, X., GRIERSON, B. A., et al., Nucl. Fusion **55** (2015) 123025.

[79] QIAN, J. P., GAROFALO, A. M., GONG, X. Z., and REN, Q. L., "Advances in the high bootstrap fraction regime on DIII-D towards the Q=5 mission of ITER steady state", submitted to Nuclear Fusion (accepted) .

[80] HANSON, J. M., BIALEK, J. M., CLEMENT, M., and FERRON, J. R., "Stability of high-performance, negative central shear discharges", submitted to Nuclear Fusion (accepted) .

[81] PRATER, R., MOELLER, C. P., PINSKER, R. I., et al., Nucl. Fusion **54** (2014) 083024.

[82] PINSKER, R. I., PRATER, R., MOELLER, C. P., and DEGRASSIE, J. S., "Experiments on Helicons in DIII-D - Investigation of the Physics of a Reactor-relevant Non-Inductive Current Drive Technology", Preprint: 2016 IAEA Fusion Energy Conference, Kyoto, paper EX/P3-22 .

[83] YOSHIDA, M., MCKEE, G. R., MURAKAMI, M., and GRIERSON, B. A., "Magnetic shear effects on plasma transport and turbulence at high electron to ion temperature ratio in DIII-D and JT-60U plasmas", submitted to Nuclear Fusion .

[84] R.B. White, M. C., Phys. Fluids **27** (1984) 2455.

[85] COLLINS, C. S., HEIDBRINK, W. W., AUSTIN, M. E., et al., Phys. Rev. Lett. **116** (2016) 95001.

[86] COLLINS, C. S., HEIDBRINK, W. W., KRAMER, G. J., and PACE, D. C., "Critical Gradient Behavior of Fast-Ion Transport from Alfven Eigenmodes Guides Predictive Models for Burning Plasmas", submitted to Nuclear Fusion .

[87] HAWRYLUK, R., An Empirical Approach to Tokamak Transport, in COPPI, B., LEOTTA, G., PFIRSCH, D., POZZOLI, R., and SINDONI, E., editors, *Physics of Plasmas Close to Thermonuclear Conditions, Volume 1*, pp. 19–46, CEC, Brussels, 1980.

[88] PODESTÀ, M., GORELENKOVA, M., and WHITE, R. B., Plasma Phys. Control. Fusion **56** (2014) 055003.

[89] KRAMER, G. J., PODESTÀ, M., HOLCOMB, C. T., and CUI, L., "Improving fast-ion confinement in high-performance discharges by suppressing Alfven eigenmodes", submitted to Nuclear Fusion (accepted) .

[90] VAN ZEELAND, M. A., HEIDBRINK, W. W., SHARAPOV, S. E., et al., Nucl. Fusion **56** (2016) 112007.

[91] VAN ZEELAND, M. A., HEIDBRINK, W. W., SHARAPOV, S. E., and SPONG, D. A., "Electron Cyclotron Heating Modification of Alfven Eigenmode Activity in DIII-D", Preprint: 2016 IAEA Fusion Energy Conference, Kyoto, paper EX/P3-24 .

[92] VAN ZEELAND, M. A., AUSTIN, M. E., GORELENKOV, N. N., et al., Phys. Plasmas **14** (2007) 056102.

[93] VAN ZEELAND, M. A., HEIDBRINK, W. W., NAZIKIAN, R., et al., Plasma Phys. Control. Fusion **50** (2008) 035009.

[94] BAYLOR, L. R., Fusion Sci. And Technol. **68** (2015) 211.

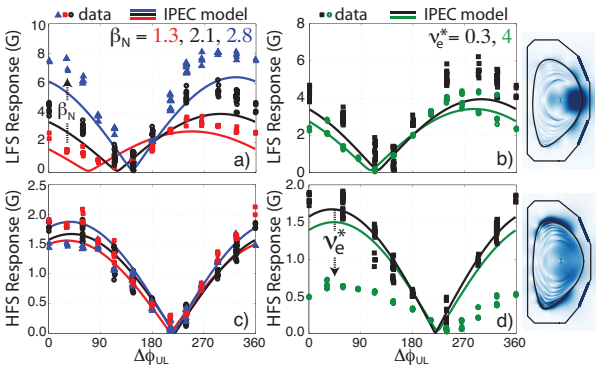

Figure 1. Plasma response amplitude to an applied $n = 2$ field as the phasing between the upper and lower I-coils is varied, at different β_N and collisionality.

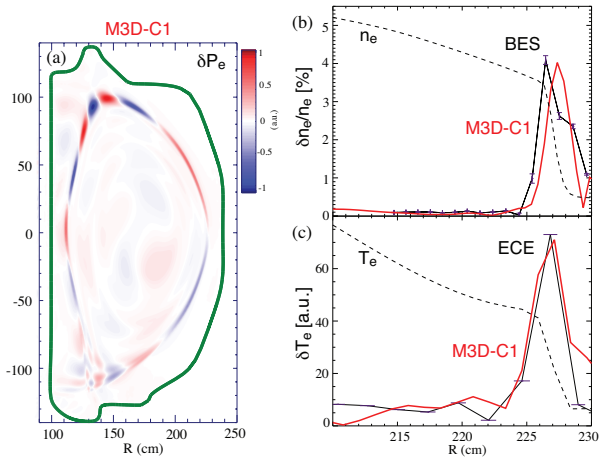

Figure 2. (a) M3D-C1 simulation of the fluctuation in the electron pressure. Comparison of fluctuations in (b) density, and (c) temperature from M3D-C1 with experimental measurements.

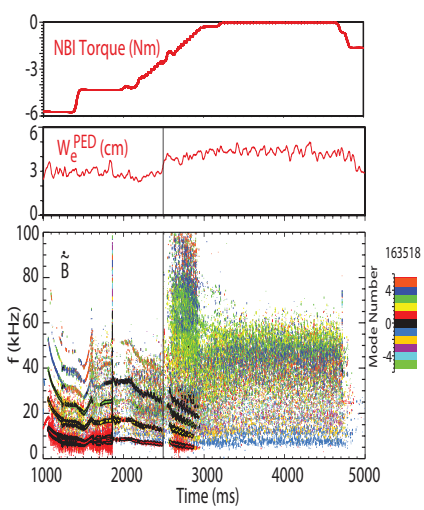

Figure 3. Pedestal width bifurcation during torque ramp down in QH-mode. (a) Neutral beam torque (from counter-injected toward balanced), (b) electron pressure pedestal width, and (c) spectrogram with toroidal modal number identification from magnetics measurements.

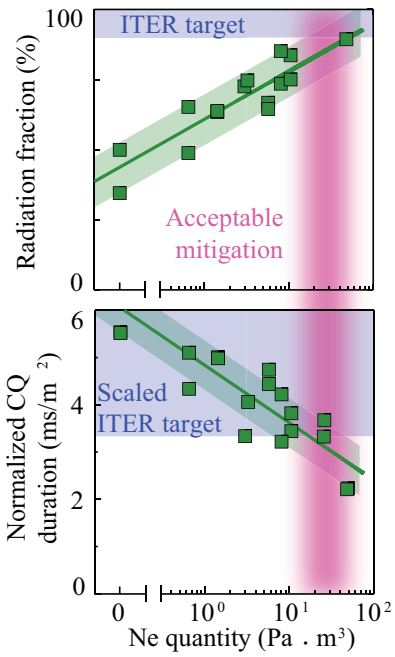

Figure 4. Radiation fraction and normalized current quench time versus neon quantity using SPI.

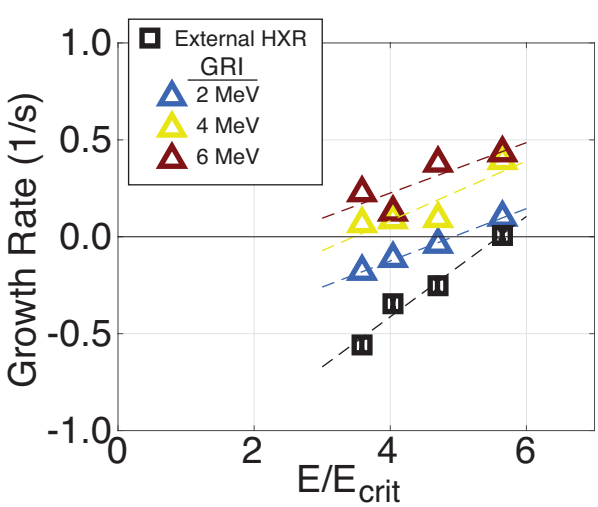

Figure 5. Energy-resolved growth rate of gamma rays from GRI as a function of electric field.

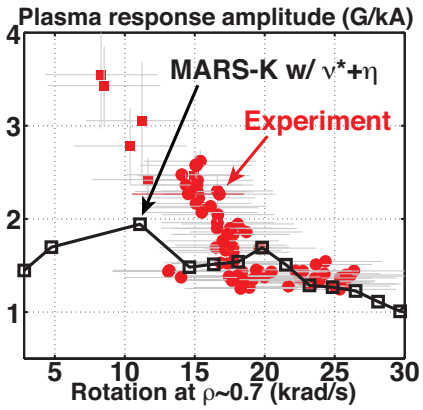

Figure 6. Plasma magnetic response amplitude to a slowly rotating (≈ 20 Hz) $n = 1$ field versus rotation, and comparison with MARS-K.

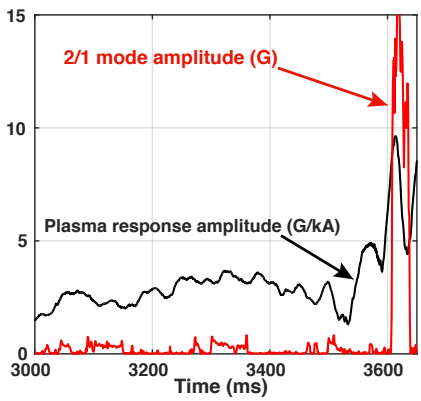

Figure 7. An increase in the plasma response measured in real-time with MHD spectroscopy is observed prior to the rapid rise of the 2/1 mode amplitude.

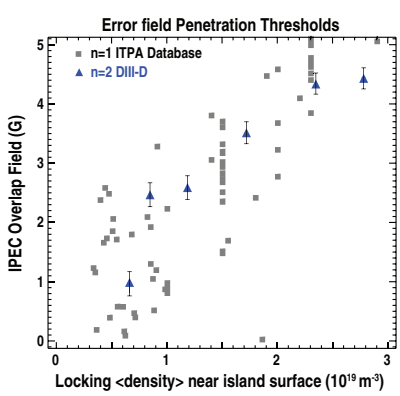

Figure 8. Density scaling of $n = 2$ locked mode threshold.

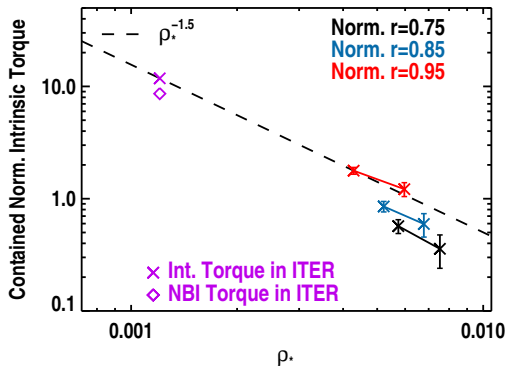

Figure 9. ρ^* scaling of intrinsic torque projected to ITER.

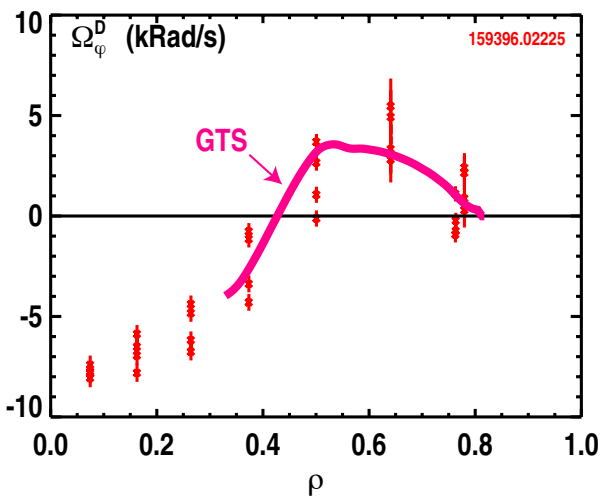

Figure 10. Comparison of measured main ion rotation with prediction from GTS gyrokinetic simulation of intrinsic drive.

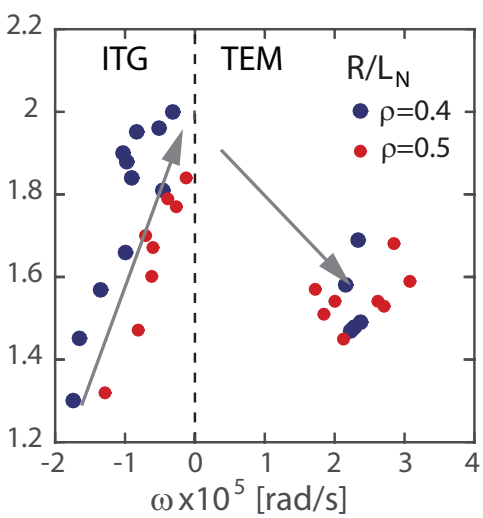

Figure 11. Degree of density peaking as a function of dominant unstable mode frequency.

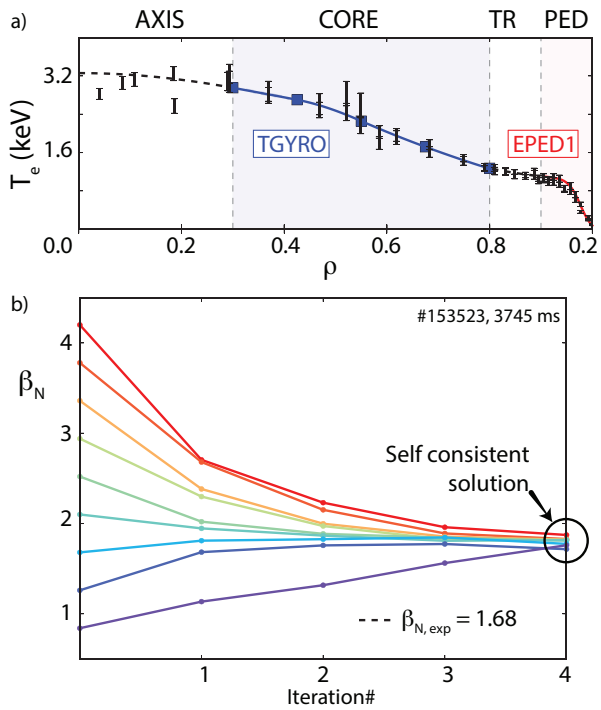

Figure 12. (a) Comparison of measured electron temperature profile with prediction from fully coupled core-pedestal transport solution using TGYRO. (b) Self-consistent solution for β_N converges toward unique, self-consistent solution independent of initial estimate.

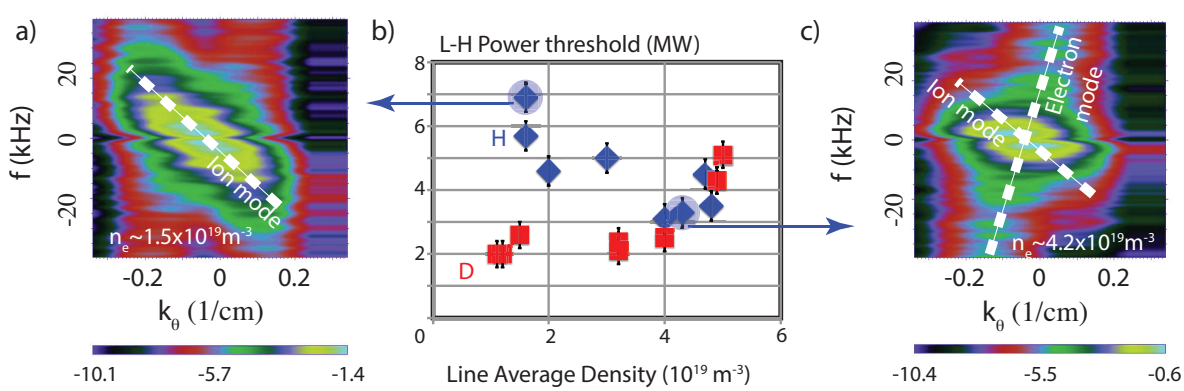

Figure 13. (a, c) Wavenumber-frequency spectrogram of density fluctuations in hydrogen plasmas, as measured by the BES diagnostic at densities 1.5×10^{19} m^{-3} and 4.2×10^{19} m^{-3}, respectively. (b) L-H power threshold as a function of density for hydrogen and deuterium plasmas.

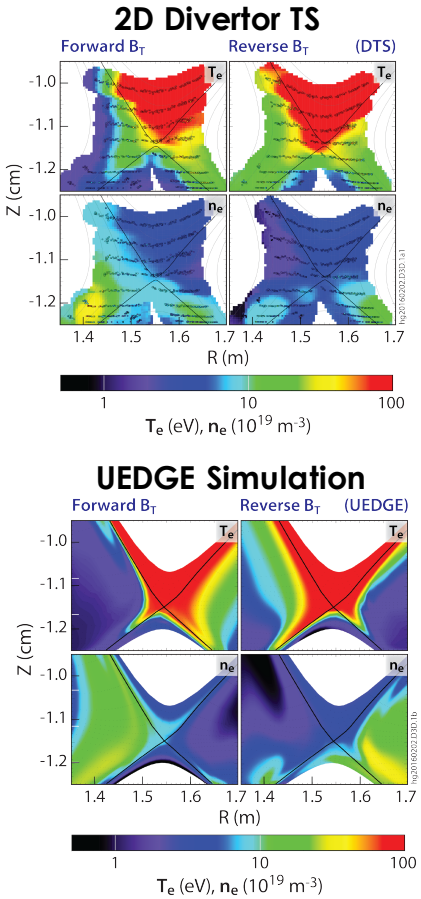

Figure 14. Comparison of measured 2D density and temperature with modeling using UEDGE, in forward and reverse B_T.

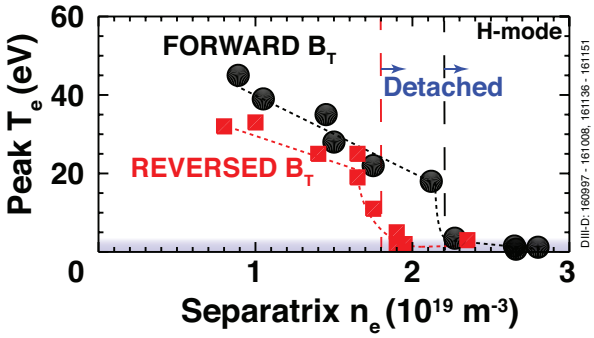

Figure 15. Comparison of threshold in density for detachment in forward and reverse toroidal field directions, indicated by a drop in the peak electron temperature at the target.

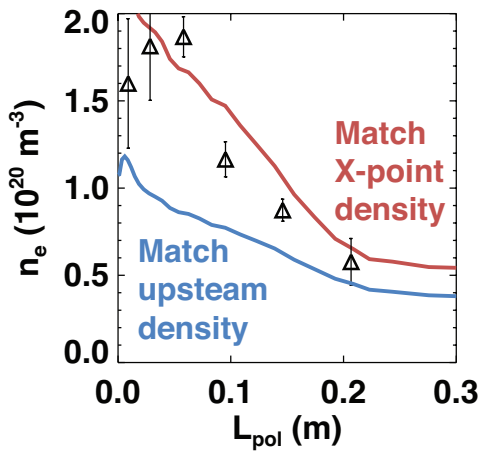

Figure 16. SOLPS predicted divertor density profile when matching the upstream density (blue) versus matching the X-point density (red), compared with the experimentally measured divertor density. When following the standard approach of matching the upstream density, the predicted divertor density is too low.

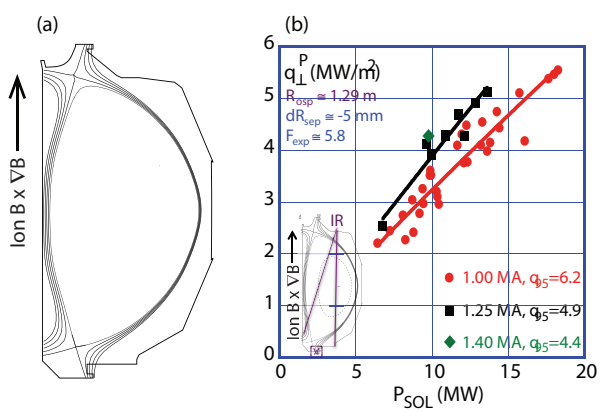

Figure 17. (a) Plasma double-null shape used for study of peak heat fluxes to the outer divertor target, including direction of $\nabla B \times B$ drift. (b) Peak heat flux in lower divertor as a function of power for different plasma currents.

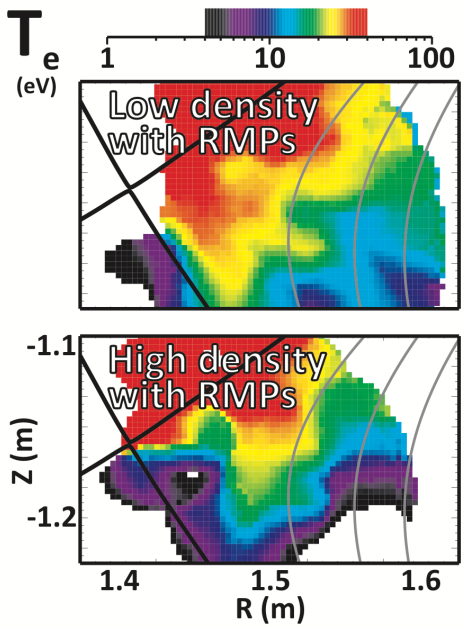

Figure 18. 2D electron temperature profile in the divertor at (a) low and (b) high density. High temperature lobes extend toward the divertor target at lower densities, but lift up and away from the target at higher density.

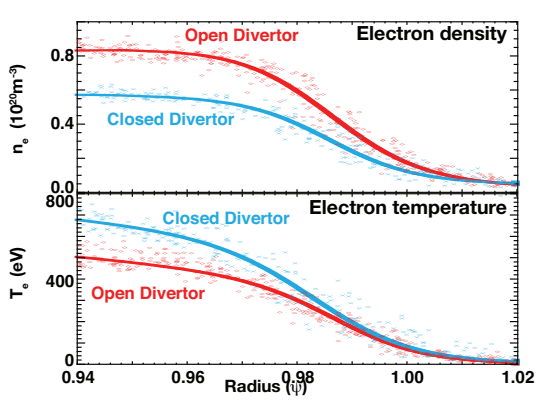

Figure 19. Comparison of density and temperature profiles between more closed versus open divertor configurations.

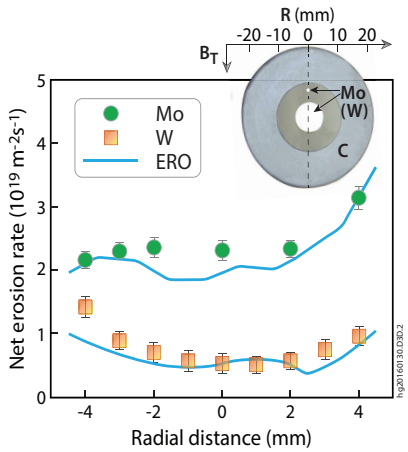

Figure 20. Experimentally measured radial profiles of net erosion rate for Mo and W and comparison with ERO modeling.

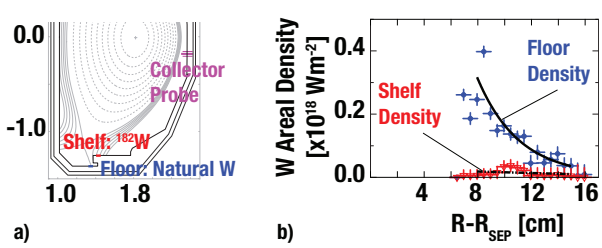

Figure 21. (a) Cross-section of lower half of DIII-D showing location of the tungsten rings and collector probe. (b) Tungsten areal density measured at the collector probe, identified by location using inductively-coupled-plasma mass spectroscopy to distinguish the different isotopes of tungsten.

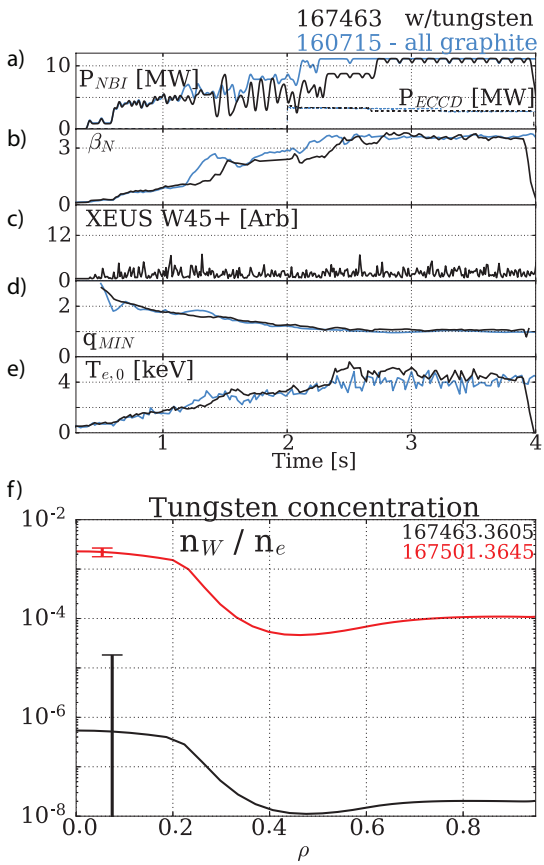

Figure 22. Comparison of hybrid discharges before and during W ring inserts: (a) Heating power; (b) β_N; (c) Spectroscopic measurement of W45+, indicating no measurable signal; (d) $q_{\min}$ evolution; and (e) central electron temperature. (f) Comparison of the tungsten concentration in this hybrid discharge with a high $q_{\min}$ discharge.

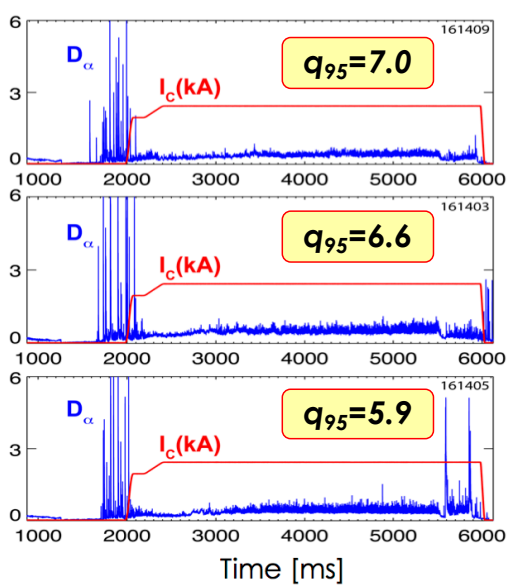

Figure 23. Demonstration of RMP ELM suppression in steady-state hybrid plasmas over a range in q_{95}.

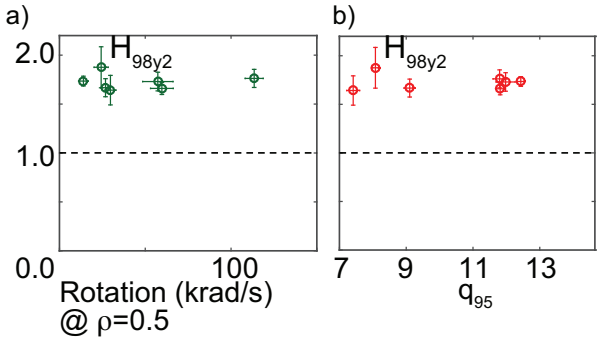

Figure 24. $H_{98(y,2)}$ confinement factor is relatively insensitive to changes in either (a) rotation or (b) q_{95} in the high β_P scenario.

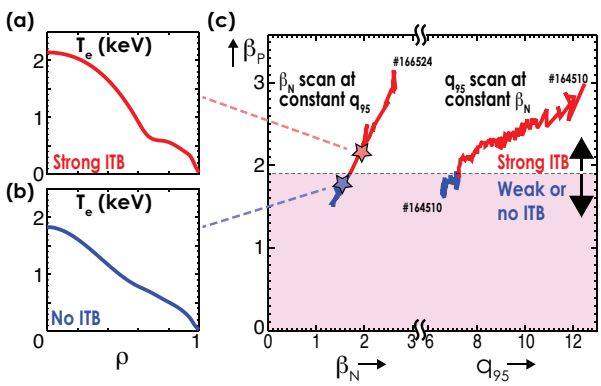

Figure 25. (a, b) Electron temperature profiles at different values of β_P, as indicated in (c) showing trajectories of β_P as either β_N or q_{95} are varied.

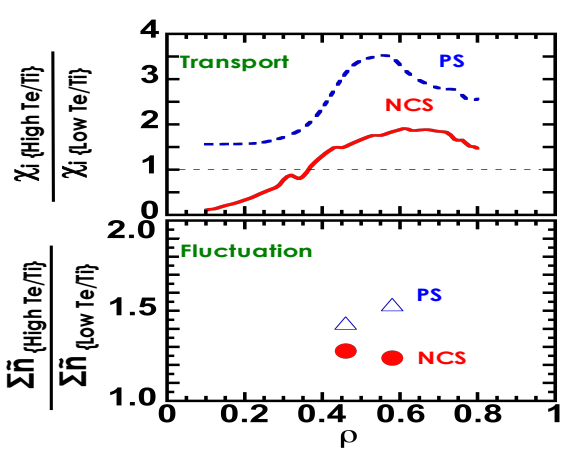

Figure 26. Relative changes in (a) ion heat diffusivity and (b) density fluctuations between high and low T_e/T_i for positive and negative central shear.

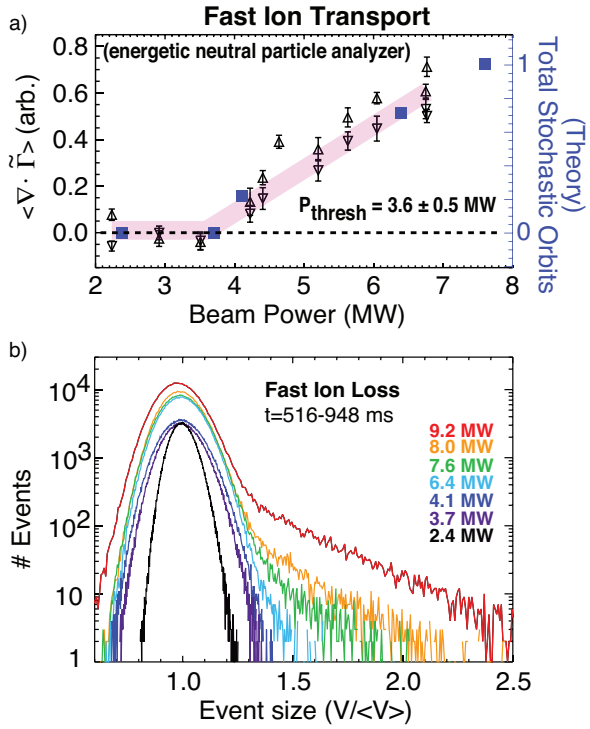

Figure 27. (a) Fast ion transport measured by energetic neutral particle analyzer as a function of applied beam power. (b) Distribution of fast ion transport events at different beam power levels.

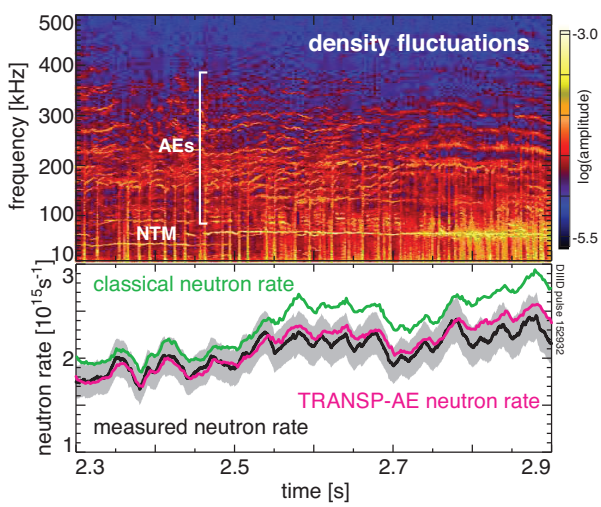

Figure 28. (a) Spectrogram of density fluctuations, showing coherent NTM at low frequency (below 100 kHz) and a wide band of coherent Alfvén Eigenmode activity at higher frequencies. (b) Comparison of measured neutron rate with classical calculation and from new phase space resolved "kick-model".

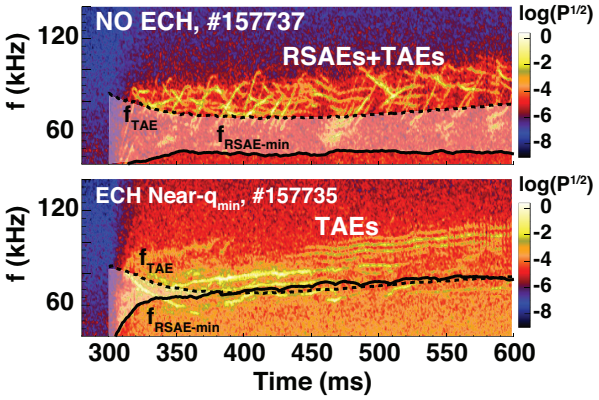

Figure 29. Density fluctuation spectrogram showing coherent Alfvén Eigenmode activity without (a) and with (b) ECH deposited near $q_{\min}$. In the case with ECH, the minimum allowed RSAE frequency exceeds the TAE frequency, and frequency sweeping RSAEs are not observed.

Appendix: The DIII-D team

G. Abla[1], T. Abrams[1], J.W. Ahn[2], E. Allen[1], S.L. Allen[3], G. Ambrosino[4], J.P. Anderson[1], N. Asakura[5], M.E. Austin[6], D. Ayala[1], S.-G. Baek[7], C.P. Balance[8], M.J. Baldwin[9], K. Barada[10], L. Bardoczi[10], J.E. Barton[11], J.L. Barton[12], E.M. Bass[13], D.J. Battaglia[13], L.R. Baylor[2], E.A. Belli[1], R. Bengtson[6], L.J. Bergsten[14], N. Bertelli[13], J. Bialek[15], M. Bobrek[2], J.A. Boedo[9], R.L. Boivin[1], N.G. Bolte[16], P. Bonoli[7], J.E. Boom[17], A. Bortolon[13], C. Bowman[18], M.D. Boyer[13], R.V. Bravenec[19], B.D. Bray[1], D.P. Brennan[20], S. Brezinsek[21], A.R. Briesemeister[2], M.W. Brookman[6], J.N. Brooks[22], D.L. Brower[10], B.R. Brown[1], E.W. Bryerton[23], D.A. Buchenauer[12], R.V. Budny[13], K.H. Burrell[1], R.J. Buttery[1], I. Bykov[9], I.L. Caldas[24], J.D. Callen[25], R.W. Callis[1], G.L. Campbell[1], G.P. Canal[1], J. Candy[1], J.M. Canik[2], L. Cao[26], M. Capella[9], A. Cappa[27], T.N. Carlstrom[1], W. Carpanese[28], D. Carralero[17], T.A. Carter[10], W.P. Cary[1], L. Casali[1], M. Cengher[1], V.S. Chan[1], C.S. Chang[13], I.T. Chapman[29], S. Che[6], J. Chen[10], J. Chen[26], M. Chen[30], X. Chen[1], Y. Chen[31], W. Choi[15], B. Choski[32], L. Chousal[9], C.P. Chrobak[1], C. Chrystal[1], R.M. Churchill[13], M.R. Cianciosa[2], D. Ciro[24], I.G.J. Classen[33], M.D. Clement[9], C.S. Collins[1], S.K. Combs[2], N. Commaux[2], C.M. Cooper[18], W.A. Cooper[34], B. Covele[1], E.N. Coviello[1], N.A. Crocker[10], B.J. Crowley[1], L. Cui[13], I. Cziegler[9], S. Danani[32], B.J. Dannels[2], E.M. Davis[7], M. De Angeli[35], P. de Marne[36], G. De Tommasi[4], P. de Vries[37], J. Decker[38], J.S. deGrassie[1], G.Z. Deng[26], A. Diallo[13], P.H. Diamond[9], A.M. Dimits[3], R. Ding[18], S.Y. Ding[26], W.X. Ding[10], J.L. Doane[1], R.P. Doerner[9], C.W. Domier[30], D. Donovan[39], C.W. Dormier[30], P. Dougherty[23], E.J. Doyle[10], D. Du[1], H. Du[40], M.C. Dunne[17], N.W. Eidietis[1], J.D. Elder[41], D. Eldon[20], R.A. Ellis[13], R.M. Ellis[3], W. Elwasif[2], D.A. Ennis[8], D.R. Ernst[7], S. Ethier[13], T.E. Evans[1], C. Favreau[8], W. Feng[26], M.E. Fenstermacher[3], N.M. Ferraro[13], J.R. Ferron[1], D. Finkenthal[42], R.K. Fisher[1], B. Fishler[1], R. Fitzpatrick[6], S.M. Flanagan[1], R.J. Fonck[25], C.R. Foust[2], E. Fredrickson[13], H. Frerichs[25], D. Fu[30], G.-Y. Fu[13], J. Galdon[36], F. Garcia[1], F.J. Garcia-Lopez[36], M. Garcia-Munoz[36], A.M. Garofalo[1], K.W. Gentle[6], S.P. Gerhardt[13], E.P. Gilson[13], F. Glass[1], P. Gohil[1], X.Z. Gong[26], N.N. Gorelenkov[13], M. Gorelenkova[13], Y. Gorelov[1], R.S. Granetz[7], T.K. Gray[2], D.L. Green[2], C.M. Greenfield[1], M. Greenwald[7], B.A. Grierson[13], R.J. Groebner[1], M. Groth[43], H.L. Grunloh[1], H.Y. Guo[1], W.F. Guo[26], J. Guterl[1], W. Guttenfelder[13], T. Guzman[1], S.H. Hahn[44], F.D. Halpern[1], M. Hansink[1], J.M. Hanson[15], S.R. Haskey[13], L. Hausammann[13], R.J. Hawryluk[13], C.C. Hegna[25], W.W. Heidbrink[16], R.R. Hernandez[9], D.N. Hill[1], D.L. Hillis[2], E. Hinson[25], S.P. Hirshman[2], M. Hoelzl[17], C.T. Holcomb[3], C. Holland[9], E.M. Hollmann[9], I. Holod[16], K. Holtrop[1], A.R. Horton[2], J. Howard[45], N. Howard[7], N.T. Howard[46], S.C. Hsu[71], F. Hu[30], X. Hu[30], Y.J. Hu[26], J. Huang[26], Y. Huang[26], A.E. Hubbard[7], J.W. Hughes[7], G.T.A. Huijsmans[13], D.A. Humphreys[1], P. Huynh[1], A.W. Hyatt[1], K. Ida[47], R. Ikeda[5], Y. In[48], S. Inagaki[49], K. Itoh[47], S.-I. Itoh[49], O. Izacard[9], V.A. Izzo[9], G.L. Jackson[1], E.F. Jaeger[50], S.C. Jardin[13], A.E. Jarvinen[3], F. Jenko[10], T.C. Jernigan[2], M.C. Jimenez-Ramos[36], C.A. Johnson[8], R.D. Johnson[1], I. Joseph[3], D.H. Kaplan[1], Y. Kawano[5], S. Kaye[13], R. Ke[73], A.G. Kellman[1], D.H. Kellman[1], K. Kim[2], J.D. King[51], A. Kirschner[21], W.-H. Ko[44], T. Kobayashi[47], E.R. Koch[1], E. Kolemen[20], M. Kostuk[1], M. Kotschenreuther[6], G.J. Kramer[13], S.I. Krasheninnikov[9], J.A. Kulchar[1], B. LaBombard[7], R.J. LaHaye[1], J. Lai[30], T. Lambot[52], M.J. Lanctot[51], R. Lantsov[10], L.L. Lao[1], A. Lasa[2], C.J. Lasnier[3], C.H. Lau[2], P. Lauber[17], M. Lauret[11], S.A. Lazerson[13], B.P. LeBlanc[13], R.L. Lee[1], X. Lee[1], M. Lehnen[37], A.W. Leonard[1], E. Li[26], G.Q. Li[26], M. Li[26], L. Liang[26], Z. Lin[16], J.B. Lister[34], C. Liu[1], F. Liu[13], H. Liu[26], J.B. Liu[26], Y.Q. Liu[29], A. Loarte[37], S.D. Loch[8], N.C. Logan[13], J. Lohr[1], J.D. Lore[2], Z.X. Lu[9], T.C. Luce[1], N.C. Luhmann[30], C.J. Luna[53], A.E.L. Lunniss[54], R. Lunsford[13], G.N. Luo[26], B.C. Lyons[18], B. Lyv[26], J.E. Maggs[10], S. Mahajan[6], R. Maingi[13], M.A. Makowski[3], M. Mamidanna[30], D.K. Mansfield[13], S. Mao[25], M. Margo[1], A. Marinoni[7], E.S. Marmar[7], L. Marrelli[55], P. Martin[55], M. Mattei[4], P. Mauzey[1], J McClenaghan[18], A. McCubbin[56], G.R. McKee[25], A.G. McLean[3], S.J. Meitner[18], J.E. Menard[13], O. Meneghini[1], W.H. Meyer[3], D. Miller[1], C.P. Moeller[1], G.J. Morales[10], S. Mordijck[57], A.L. Moser[1], R.A. Moyer[9], D. Mueller[13], T.L. Munsat[31], M. Murakami[2], C. Murphy[1], C.M. Muscatello[1], C.E. Myers[13], L. Myrabo[58], A. Nagy[13], M. Nakata[47], A.B. Navarro[10], G.A. Navratil[15], R. Nazikian[13], G. Neu[17], X. Nguyen[10], M. Nocente[59], S. Noraky[1], J.-M. Noterdaeme[17], R.E. Nygren[12], M. O'Mullane[60], Y. Oda[5], S. Ohdachi[47], M. Okabayashi[13], K.E.J. Olofsson[18], M. Ono[61], D.M. Orlov[9], T.H. Osborne[1], L. Owen[2], N.A. Pablant[13], R. Paccagnella[55], D.C. Pace[1], C.K. Pan[26], J.-K. Park[13], J.M. Park[2], C. Parker[1], S.E. Parker[31], K.L. Parkin[52], P.B. Parks[1], G. Pautasso[17], C.J. Pawley[1], C. Paz-Soldan[1], W.A. Peebles[10], B.G. Penaflor[1], J. Penna[7], E.A.D. Persico[16], T.W. Petrie[1], C.C. Petty[1], Y. Peysson[38], A.-V. Pham[30], T. Phan[30], A.Yu. Pigarov[9], D. Pince[1], R.I. Pinsker[1], P. Piovesan[55], L. Piron[55], R.A. Pitts[37], M. Podesta[13], F. Poli[13], D. Ponce[1], M. Porkolab[7], G.D. Porter[3], R. Prater[1], J.P. Qian[26], C. Rapson[17], S. Ratynskaia[62], J.M. Rauch[1], P. Raum[63], G. Raupp[17], C. Rea[7], A.H. Reiman[13], H. Reimerdes[34], M.L. Reinke[2], Q.L. Ren[26], X. Ren[30], T.L. Rhodes[10], P. Ricci[34], J.E. Rice[7], L. Riford[11], M.A. Riso[64], G. Riva[35], P. Rodriguez-Fernandez[7], M. Rodriguez-Ramos[36], T.D. Rognlien[3], A. Romosan[65], A.L. Roquemore[13], J.C. Rost[7], W.L. Rowan[6], D.L. Rudakov[9], D. Ryan[29], D.D. Ryutov[3], K. Sakamoto[5], A. Salmi[66], B. Sammuli[1], C.M. Samuel[3], L. Sanchis-Sanchez[36], C.F. Sang[40], D.P. Schissel[1], L. Schmitz[10], O. Schmitz[25], E. Schuster[11], J.T. Scoville[1], S.K. Seal[2], M.W. Shafer[2], S.E. Sharapov[29], S.K. Sharma[32], H. Sheng[67], M. Shephard[68], L. Shi[13], W. Shi[11], S. Shiraiwa[7], D. Shiraki[2], A. Shoshani[65], H. Si[26], D. Smith[25], S.P. Smith[1], A. Snicker[17], J.A. Snipes[37], P.B. Snyder[1], W.M. Solomon[1], A.C. Sontag[2], V.A. Soukhanovskii[3], A.G. Spear[30], D. Spong[2], W.M. Stacey[70], G.M. Staebler[1], L. Stagner[16], P.C. Stangeby[41], E. Startsev[13], R. Stemprok[1], J. Stillerman[7], D.P. Stotler[13], E.J. Strait[1], X. Sun[26], C. Sung[10], W. Suttrop[17], Y. Suzuki[47], R. Sweeney[15], S. Taimourzadeh[16], K. Takahashi[5], T. Tala[66], H. Tan[26], W.M. Tang[13], R.L. Tanna[32], D. Taussig[1], G. Taylor[13], N.Z. Taylor[18], P. Taylor[1], T.S. Taylor[1], J.L. Terry[7], D.M. Thomas[1], K.E. Thome[18], A. Thorman[45], A.J. Thorton[29], A. Tinguely[7], B.J. Tobias[13],

P. Tolias[62], J.F. Tooker[1], H. Torreblanca[1], A.C. Torrezan[1], W. Treutterer[17], D.D. Truong[25], D. Tskhakaya[69], C.K. Tsui[9], F. Turco[15], A.D. Turnbull[1], G.R. Tynan[9], M.V. Umansky[3], E.A. Unterberg[2], P. Valanju[6], E. Valeo[13], M.A. VanZeeland[1], B.S. Victor[3], R. Vieira[7], F.A. Volpe[15], M.S. Vorenkamp[13], M.R. Wade[1], J. Walk[7], M.I. Walker[1], G. Wallace[7], R.E. Waltz[1], W.R. Wampler[12], B.N. Wan[26], W. Wan[31], G. Wang[10], H. Wang[26], H.Q. Wang[18], L. Wang[26], Q. Wang[74], W.X. Wang[13], X. Wang[57], Z. Wang[46], Z.R. Wang[13], C. Wannberg[10], J.G. Watkins[12], W.P. Wehner[11], A.S. Welander[1], A.E. White[7], R.B. White[13], R.S. Wilcox[2], T. Wilks[7], H.R. Wilson[54], A. Wingen[2], A. Winter[37], S. Wolfe[7], C.P.C. Wong[1], G.M. Wright[7], J. Wright[7], K.J. Wu[65], W. Wu[1], S. Wukitch[7], B.J. Xiao[26], W.W. Xiao[75], Y. Xie[26], G.S. Xu[26], X. Xu[3], Z. Yan[25], S. Yang[40], M. Yoshida[5], L. Yu[6], Q. Yuan[26], M. Zach[2], P. Zanca[55], Q. Zang[26], S. Zemedkun[31], L. Zeng[10], B. Zhang[26], F. Zhang[68], X. Zhao[9], Y. Zhao[72], Y.B. Zhu[16]

Affiliations

[1]General Atomics
[2]Oak Ridge National Laboratory
[3]Lawrence Livermore National Laboratory
[4]CREATE/Seconda Universit di Napoli
[5]National Institutes for Quantum and Radiological Science and Technology
[6]University of Texas Austin
[7]Massachusetts Institute of Technology
[8]Auburn University
[9]University of California San Diego
[10]University of California Los Angeles
[11]Lehigh University
[12]Sandia National Laboratory
[13]Princeton Plasma Physics Laboratory
[14]Dartmouth College
[15]Columbia University
[16]University of California Irvine
[17]Max-Planck-Institut fr Plasmaphysik
[18]Oak Ridge Associated Universities
[19]Fourth State Research
[20]Princeton University
[21]Forschungszentrum Jlich GmbH
[22]Purdue University
[23]Virginia Diodes, Inc.
[24]Universidade de So Paulo
[25]University of Wisconsin-Madison
[26]Institute of Plasma Physics, Chinese Academy of Sciences
[27]Laboratorio Nacional de Fusion-CIEMAT
[28]Politecnico di Milano
[29]CCFE Fusion Association
[30]University of California Davis
[31]University of Colorado
[32]Institute for Plasma Research, India
[33]Dutch Institute for Fundamental Fusion Energy Research
[34]CRPP Lausanne
[35]Instituto di Fisica del Plasma
[36]University of Seville
[37]ITER Organization
[38]CEA
[39]University of Tennessee
[40]Dalian University of Technology
[41]University of Toronto
[42]Palomar Scientific Instruments
[43]Aalto University
[44]NFRI
[45]Australia National University
[46]Oak Ridge Institute for Science and Education (ORISE)
[47]National Institute for Fusion Science
[48]FAR-TECH
[49]Kyushu University
[50]XCEL Engineering, Inc.
[51]US Department of Energy
[52]Carnegie Mellon University
[53]Arizona State University
[54]University of York
[55]Consorzio RFX
[56]Hope College
[57]College of William and Mary
[58]Lightcraft Technologies, Inc.
[59]Universita degli Studi di Milano-Bicocca
[60]University of Strathclyde
[61]The Graduate University for Advanced Studies (SOKENDAI)
[62]KTH Royal Institute of Technlogy
[63]Virginia Tech
[64]State University of New York-Buffalo
[65]Lawrence Berkeley National Laboratory
[66]Association EURATOM-Tekes
[67]Peking University
[68]Rensselaer Polytechnic Institute
[69]University of Innsbruck
[70]Georgia Tech
[71]Los Alamos National Laboratory
[72]Suzhou University
[73]Tsinghua University
[74]Zhejiang University
[75]Southwestern Institute of Physics